Journal of Fluids and Structures 100 (2021) 103175

Contents lists available at ScienceDirect

Journal of Fluids and Structures

journal homepage: www.elsevier.com/locate/jfs

Effects of tunable stiffness on the hydrodynamics and flow features of a passive pitching panel

HaiZhou Hu [a], Junshi Wang [b], Yankui Wang [a], Haibo Dong [b,*]

[a] Ministry-of-Education Key laboratory of Fluid Mechanics, Beihang University, Beijing 100191, China
[b] Department of Mechanical & Aerospace Engineering, University of Virginia, Charlottesville, VA 22904, United States of America

ARTICLE INFO

Article history:
Received 15 May 2020
Received in revised form 22 August 2020
Accepted 21 October 2020
Available online 7 November 2020

Keywords:
Pitching panel
Bio-inspired propulsion
Tunable stiffness

ABSTRACT

Three-dimensional numerical simulations are carried out to study the hydrodynamic performance and flow features of a bio-inspired underwater propulsor. The propulsor is constituted by a passive pitching panel. The leading edge of the panel is prescribed under a periodic heaving motion while the panel pitches passively due to the employing of a stiffness-lumped torsional spring at the leading edge. Effects of the torsional spring stiffness have been put emphases on. A real-time tunable stiffness strategy is presented and employed in the study. We first study the passive pitching effects on the hydrodynamics and flow features of the panel using a series of constant stiffness and then we study the tunable stiffness effects using cosinusoidal curve based waveforms, in which the effects of phase difference (φ) between the stiffness profile and the oscillation motion and as well as the effects of stiffness fluctuation amplitude (G_k) are investigated, respectively. The stiffness profile beneficial for propulsion efficiency is further applied to cases with different oscillation amplitudes. A high-fidelity immersed boundary method based direct numerical simulation (DNS) solver is employed to acquire the fluid dynamics and to simulate the flow. The panel passive pitching motion is solved by coupling the DNS flow solver and the Euler rigid body dynamic equation. Results show that for the constant stiffness cases, the panel generates sinusoidal-like pitching motion, and in certain stiffness range, flexibility could benefit efficiency while holding some extent of stiffness could enhance the thrust. For the tunable stiffness cases, it is found that both the mean thrust and propulsive efficiency improved when the stiffness change is in-phase with the heaving motion ($\varphi = 0°$). The largest mean thrust is found at $\varphi = 120°$. The wake profile shows that in the constant stiffness cases and $\varphi = 120°$ case, the panel in each cycle generates a pair of elongated and twisted vortex tubes, the vortex tubes in each pair interconnected with each other and induces unprofitable interactions. While in the $\varphi = 0°$ case the panel generates a pair of round and closed vortex loops in each cycle and the vortex loops separated directly after they have been detached from the panel and thus avoided the unprofitable vortex interactions. The stiffness fluctuation amplitude (G_k) effects study (all employing the in-phase stiffness profile) shows that all the three tested cases ($G_k = 0.25G_0, 0.5G_0, 0.75G_0$) acquired thrust and efficiency enhancement while the $G_k = 0.5G_0$ case acquired the largest efficiency benefit and the $G_k = 0.75G_0$ case had the largest thrust. Wake profiles show entire vortex loops may not be formed when G_k is small while larger G_k may affect the arrangement of the vortex loops thus may generate unprofitable vortex interactions. The results of cases with motions with variable oscillating amplitudes (A^*) show employing the real-time altering stiffness profile ($\varphi = 0°, G_k = 0.5G_0$) improves the propulsion performance in a certain range of A^* ($0.4 \leq A^* \leq 0.8$). Results from this paper demonstrated the

* Corresponding author.
E-mail address: hd6q@virginia.edu (H. Dong).

https://doi.org/10.1016/j.jfluidstructs.2020.103175

potential of using real-time tunable stiffness in the design of passive pitching propulsors of underwater vehicles that pursue higher performance.

1. Introduction

Fishes possess remarkable swimming performance such as high swimming speed, high efficiency and enduring swimming ability. Most of these fishes are found to swim by bending their aft-body and pitching their caudal fin, which is thought to be the major way of providing thrust. Despite the active bending or pitching which is actuated by muscle, passive morphing or pitching mechanism is widely found in fish swimming and insect flight in nature (Bergou et al., 2007; Daniel and Combes, 2002; Fish et al., 2006). Previous research has shown that these passive morphing or rotation may be beneficial for the sake of improving efficiency, however, in the case of a robot that uses rigid panel as a propulsor, in which the flexibility is lumped at the joint or leading edge of the panel, employing completely passive pitching motion will decrease mechanical complexity and reduce system mass (Wood, 2008). On the other hand, evidence in nature shows that stiffness of propulsors can be actively controlled for pursuing better performance (Adams and Fish, 2019). Whereas, in recent researches, the passive rotating propulsors are all employing constant stiffness. The research about passive pitching propulsor which employs real-time tunable stiffness is scarce. The main goal of this paper is to study the tunable stiffness effects on a bio-inspired passive pitching propulsor.

The stiffness-lumped passive pitching mechanism has been studied by some researchers in robot design or fluid mechanism studies. These studies are related to both insect flying and fish swimming. Ishihara studied the lift generation in the crane fly's flapping wing motions using a dynamically scaled model that employs a plate spring on the wing joint. High angle of attack was maintained passively during the flapping motion and sufficient lift was generated to support the insect weight (Ishihara et al., 2009). Whitney and Wood used the theoretical method to study the aeromechanics of passive rotation in flapping flight in which the aerodynamics is predicted by a blade-element model and the passive rotation is acquired by coupling the blade-element model and rigid body dynamics equation (Whitney and Wood, 2010). Zhu et al. (2019) used two joints to mimic the lateral bending in the tuna fish swimming in his design of a tuna-like robot which achieved a maximum swimming speed of 4.0 body lengths (BL) per second. Note that most of the documented fish-like robots can only achieve body velocities of 0.25∼1.5 BL/s. Zhu uses one joint to connect the actuation system and posterior support structure and employs another joint to connect the posterior support structure and the caudal fin. Elastic bands were attached to link the posterior support structure and the caudal fin, so the posterior joint could rotate passively due to the interaction between the elastic bands, fluid pressure, and structural inertia. The research mainly talked about the capability of high-frequency swimming and swimming performance such as midline kinematics, speed and cost of transport (COT), etc. Fluid dynamics and flow features about this kind of stiffness-lumped flapping panels have been studied by some researchers. Zhong et al. (2019) studied the interaction between dorsal and caudal fin using a tuna-inspired platform which also employs this kind of passive pitching mechanism in the peduncle part of the fish just like Zhu et al. (2019) did in the tuna robot. Some other researchers using this kind of passive pitching model to study the aero/hydrodynamics and flow features about flapping wing or panels can be found in (Moore, 2014; Wang et al., 2018; Zeyghami et al., 2018; Zhong et al., 2017).

However, as mentioned above, the previous studies all employ constant stiffness. We here hypothesize that particularly controlling the stiffness in this kind of stiffness-lumped passive pitching panel may improve the thrust or efficiency. We first employ a series of constant stiffness to study the constant stiffness effects on the propulsion performance of the panel, then we study the real-time tunable stiffness effects using sinusoidal curve based waveforms. Effects of the phase difference between the stiffness profile and the oscillation motion and as well as the effects of stiffness fluctuation amplitude (G_k) are investigated. A high-fidelity immersed boundary method based direct numerical simulation (DNS) solver is employed to simulate the flow and hydrodynamics and the pitching motion is solved by coupling the flow solver and the Euler rigid body dynamic equation.

2. Problem definition and methods

2.1. Problem definition

The current research employs a bio-inspired trapezoidal panel. The aspect ratio (AR) of the panel is defined as the ratio of the square of the longer base of the panel to the area of the panel (L^2/S, where L is the longer base, and S is the area) and is set to be 2.025 in the current work. A virtual torsional spring is employed at the leading edge to connect the actuation motion and the panel. The leading edge undergoes a prescribed harmonic oscillating motion which is described by Eq. (1)

$$x(t) = \frac{A_x}{2}\cos(2\pi f t) \tag{1}$$

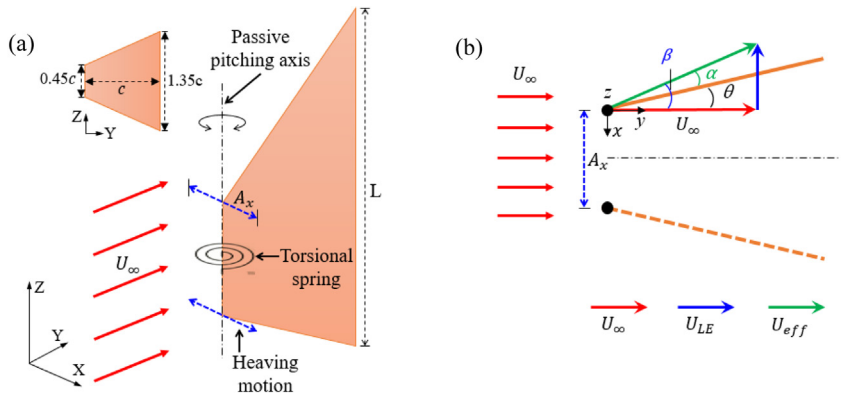

Fig. 1. (a) Schematic of the motion; (b) top view and definition of pitch angle θ.

where A_x denotes the oscillation peak to peak amplitude, f denotes the oscillation frequency and t denotes time. The panel pitches passively due to the interaction from fluid dynamics, elastic force and the structure inertia force. The pitch angle θ is defined as the angle between the panel chord and the stream-wise direction. The schematics of the motion and definition of the pitch angle are shown in Fig. 1.

The pitch motion is solved by coupling the fluid dynamics solver and the Euler dynamic equation under the non-inertial reference frame which is described as Eq. (2)

$$I_{zz}\dot{\omega}_z = M_{fluids} + M_{elastic} + M_{inertia} \tag{2}$$

where I_{zz} is the moment of inertia of the panel about the z-axis (leading edge) under the moving frame xyz that is shown in Fig. 1.(b). The origin of the moving frame is located at and moves with the leading edge and the x, y-direction follows the X, Y-direction of the globe frame that is shown in Fig. 1.(a) and all frames follow the right-hand rule. $\dot{\omega}_z$ is the angular acceleration of the pitch angle. On the right-hand side of Eq. (2), M_{fluids} denotes the torque about the pitching axis from the fluid dynamics, which is obtained by surface integration of pressure and shear stress; $M_{elastic}$ denotes the torque about the pitching axis from the elastic feedback of the torsional spring which can be written as

$$M_{elastic} = -G\theta \tag{3}$$

where G is the stiffness of the spring and θ is pitch angle.

$M_{inertia}$ is the torque about the pitching axis from the panel structure inertia force due to the acceleration of the moving frame and is written as

$$M_{inertia} = -m(\boldsymbol{r}_C \times \boldsymbol{a}_o) \cdot \boldsymbol{l} \tag{4}$$

where m denotes the mass of the panel and $\boldsymbol{r}_C$ is the vector of the mass center from the origin of the moving frame, while $\boldsymbol{a}_o$ is the acceleration of the origin of the moving frame and $\boldsymbol{l}$ is the pitching axis vector (along the z-direction of the moving frame).

2.2. Scaling and non-dimensionalization

To build dynamic similarity, five dimensionless numbers are used in the present research: Reynolds number, reduced frequency, Cauchy number, Mass number, and the ratio of oscillation amplitude to the chord. The Reynolds number denotes the ratio of fluid inertia force to viscous force and is defined as $Re = Uc/v$, where U is the far coming flow velocity, c is the chord length and v is the kinematic viscosity. Reduced frequency $k = fc/U$ is used to represent the non-dimensional oscillation frequency, where f is oscillation frequency. The Cauchy number is defined here as $Ch = \rho(U^2 + V^2)c^3/G$, which denotes the ratio of fluid dynamic pressure to the elastic force and is used to express the non-dimensional stiffness of the torsional spring. $V = \pi f A_x$ stands for the maximum speed of the oscillation motion, ρ is the fluid density and G is the torsional spring stiffness. The Mass number is defined as $M = m_p/m_f = (\rho_p \bar{e})/(\rho c)$, where m_p denotes the mass of the plate and m_f denotes the fluid added mass; ρ_p is the density of the panel while $\bar{e}$ is the thickness of the plate. The ratio of oscillation amplitude to the chord is defined as $A^* = A_x/c$, where A_x is the leading edge amplitude. Similar definitions can be found in (Floryan et al., 2017; Ishihara et al., 2009; Sum Wu et al., 2019; Zeyghami et al., 2018).

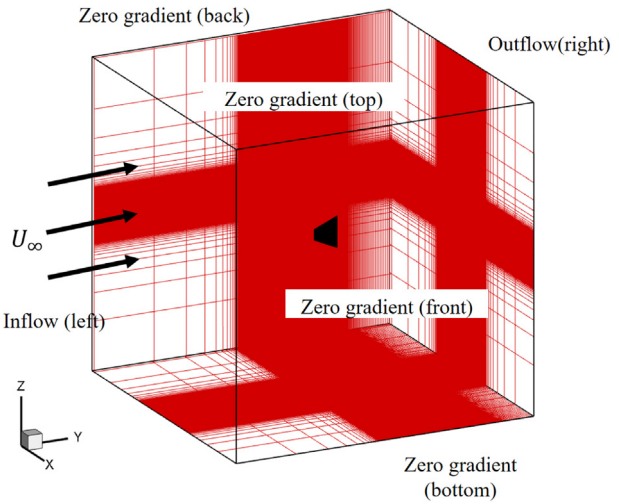

Fig. 2. Schematic of the computational domain, mesh and boundary conditions.

2.3. Propulsion performance evaluation

Thrust, lateral force, and hydrodynamic power as well as hydrodynamic efficiency are considered in the propulsion performance evaluation. The thrust coefficient is defined as $C_T = F_T/(0.5\rho U^2 S)$, where F_T is thrust and S is the area of the panel. The lateral force coefficient is defined as $C_L = F_L/(0.5\rho U^2 S)$, where F_L is lateral force. The hydrodynamic power coefficient is calculated as $C_{PW} = \oint -\left(\overline{\overline{\boldsymbol{\sigma}}} \cdot \boldsymbol{n}\right) \cdot \boldsymbol{V} \cdot ds/(0.5\rho U^3 S)$, where $\overline{\overline{\boldsymbol{\sigma}}}$ and $\boldsymbol{V}$ are the stress tensor and velocity vector of the fluid adjacent to the model surface, respectively, and $\boldsymbol{n}$ is the normal vector of each discretized model surface. The hydrodynamic efficiency is defined as $\eta = \overline{C_T}/\overline{C_{PW}}$, where $\overline{C_T}$ and $\overline{C_{PW}}$ are cycle-averaged thrust coefficient and hydrodynamic power coefficient.

2.4. Numerical method

The fluid dynamics and flow features are solved by a high fidelity immersed-boundary-method based direct numerical simulation (DNS) solver. The incompressible flow is governed by the three dimensional Navier–Stokes equations which can be written in the following tensor form,

$$\frac{\partial u_i}{\partial x_i} = 0; \ \frac{\partial u_i}{\partial t} + \frac{\partial u_i u_j}{\partial x_j} = -\frac{\partial p}{\partial x_i} + \frac{1}{Re}\frac{\partial^2 u_i}{\partial x_j \partial x_j} \tag{5}$$

where u_i (i = 1,2,3) are velocity components and p is fluid pressure. Re is Reynolds number. A second-order central difference scheme is employed on the non-uniform Cartesian grids in space discretization and a fractional step method is used in integration in time scale. The solver has been widely employed in low-Reynolds number flow problems with complex boundary motions, especially in flying animals and aquatic animals flow simulations (Dong et al., 2009; Li and Dong, 2016; Liu et al., 2017; Wang et al., 2019; Khalid et al., 2020; Wang et al., 2020). Details and validations of the solver can be found in previous works (Li and Dong, 2017; Li et al., 2015; Mittal et al., 2008; Wan et al., 2015).

The computational domain has a size of 15c×15c×16c in X, Y, Z direction respectively, where c denotes the cord length of the panel. Grids independence study was carried out in the tests. Three sets of grids with mesh resolution of 160×224×112, 224×288×144, 256×320×176 respectively in X, Y, Z direction are used in the tests. For simplicity, the above grids are named coarse mesh, medium mesh and dense mesh apart. The mesh employs a non-uniform strategy in discretizing the space. Dense regions are employed near the panel and also the following so-called wake region. In ahead of the dense region as well as in the sideward, a fast stretching grid strategy is employed to minimize the total grids number so it can decrease the computational costs. The total grids numbers of the above coarse, medium and dense meshes are about 4.01 million, 9.29 million and 14.42 million respectively. A schematic view of the grids layout is shown in Fig. 2. The upstream boundary is set to velocity inflow boundary with constant inflow velocity. The downstream boundary is set to outflow boundary that allows the vortices to convect out with no reflections. The lateral boundaries are set to be zero-gradient boundaries. A homogeneous Neumann boundary condition is employed for pressure at all boundaries.

Fig. 3 shows the comparison of the panel thrust coefficients for the grid independence study. The parameters for the tested case is set as $k = 1$, $Re = 500$, $Ch = 0.181$, $M = 0.1$, $A^* = 0.4$. The figure takes the hydrodynamic results of one full cycle. It can be seen that the fine mesh result and the medium mesh result matched very well and both the cycle-averaged

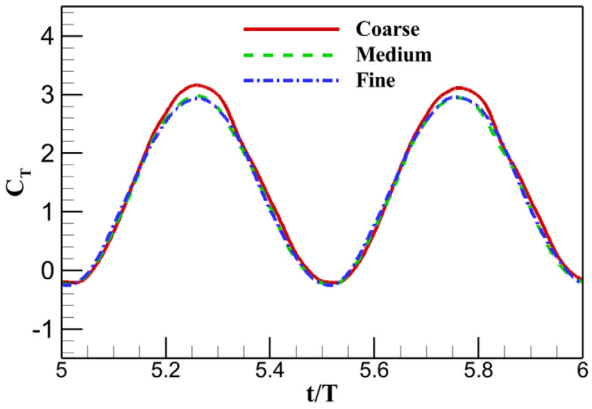

Fig. 3. Comparison of the thrust coefficient for the grid independence test. The grids-resolutions for the test are 160×224×112 (coarse mesh) with minimum grid size $\Delta_{\min} = 0.0029c$, 224×288×144 (medium mesh) with $\Delta_{\min} = 0.0021c$, and 256×320×176 (fine mesh) with $\Delta_{\min} = 0.0016c$.

thrust difference and the peak thrust difference are less than 1.6%. So it proves the hydrodynamic result is independent of the grid when the mesh reaches the medium mesh level. The medium mesh is adopted in the following cases in the study.

2.5. Validation

Other than the validations given by the literature, here we validate the solver capability by comparing the wake structures of a pure pitching panel between the numerical result and experimental result (King et al., 2018). The panel has an aspect ratio of 4.17 and pitches sinusoidally around its leading edge. The amplitude is 7.5° and frequency equals to 1. The Strouhal number ($St = fA/U$, where A is the trailing edge amplitude) is adjusted by changing the incoming flow velocity. The Reynolds numbers from experimental tests range from 4800∼16000, whereas due to the memory limit of the simulation computer, the Reynolds number from the simulations is set to 4000 since higher Reynolds number simulation requires denser mesh which surpasses the memory capability. The mesh resolution is 224×416×288 (total grids number is 26.8 million). Three Strouhal number cases (St = 0.17, 0.37, 0.56) are tested. The wake structures are plotted in Fig. 4.

We can see that even though the numerical result and experimental result have certain differences in Reynolds number, the simulation results captured most of the flow features that appeared in the experiments. At low Strouhal number (St = 0.17), the wake comprehension in span-wise direction is not obvious and the vortex loops look like ladders convecting downstream and have large spacing between each vortex tubes. At medium Strouhal number (St = 0.37), the spanwise comprehension becomes evident and the vortex tubes become twisted and interconnect with each other as they convect downstream. The spacing between each spanwise vortex tubes become smaller compared with the St = 0.17 case. At the largest Strouhal number (St = 0.56), the comprehension effect becomes more obvious and the vortexes lose coherence as soon as they are shed nevertheless in the simulation result the vortexes still hold coherence for about 0.5 cord length distance downstream of the panel which may because the viscous effect is more significant since the Reynolds number is a little bit lower than that of the experimental result.

3. Results

3.1. Constant stiffness effects

3.1.1. Kinematics and hydrodynamics

In this section, a series of constant stiffness tests are carried out to study the stiffness (constant) effects on the propulsion performance. In order to study the effects of the stiffness specifically, the reduced frequency, Reynolds number, Mass number and oscillation amplitude are kept the same ($k = 1, Re = 500, M = 0.1, A^* = 0.4$), while the Cauchy numbers are set as the following values: Ch = 0.089, 0.133, 0.178, 0.222, 0.267, 0.311, 0.356, 0.4, 0.445, 0.051.

Table 1 gives the cycle-averaged hydrodynamic performance ($\overline{C_T}$, $\overline{C_{PW}}$, η) for different stiffness cases. A wide range of stiffness cases were carried out in order to find the thrust and efficiency peak. From the results, it can be seen that when $Ch = 0.178$ the panel receives the maximum cycle averaged thrust among the varied stiffness cases while the Ch = 0.4 case acquires the maximum hydrodynamic efficiency. Note that according to the definition of the Cauchy number in Section 2.2, the larger the Cauchy number denotes the more flexible torsional spring. So it seems that the flexibility could help the panel gain more efficiency while possessing a certain extent of stiffness could help to generate more thrust.

Fig. 5 shows the time history of the passive pitching kinematics and hydrodynamic performance in one full cycle for the different stiffness cases (for simplicity, only 3 cases are plotted in the figure: the stiffest one, the maximum cycle-averaged

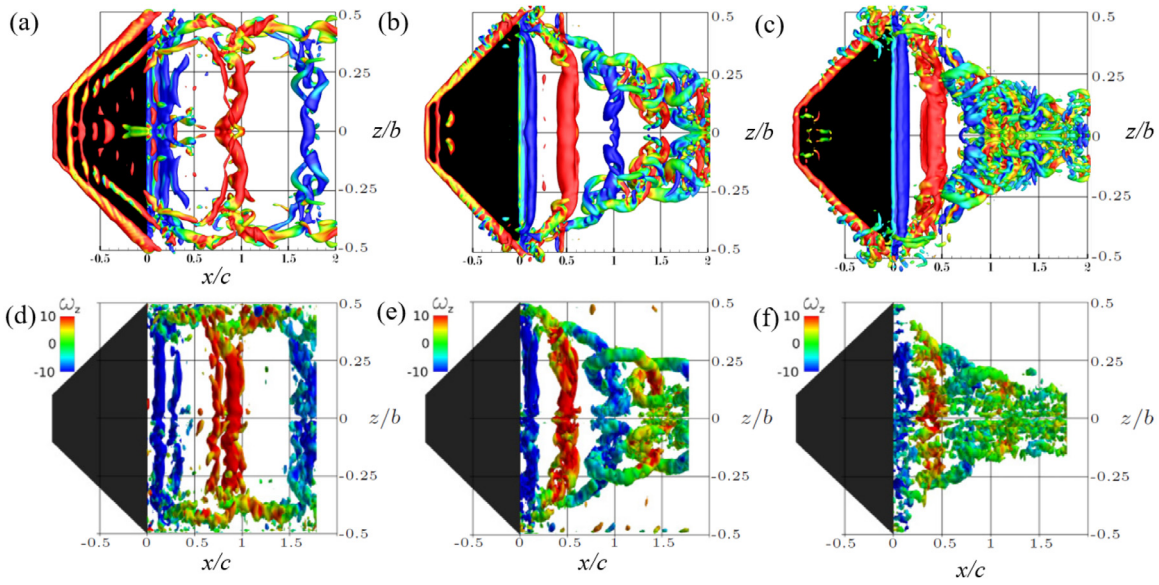

Fig. 4. Wake comparisons between the simulation results and Experimental results. The three dimensional wake structure is visualized by isosurface of Q criterion at level of 1% Q_{max} for each St. The isosurface is colored by ω_z. (a), (d) St = 0.17; (b), (e) St = 0.37; (c), (f) St = 0.56. The first row is from the simulation results and the second row is from the experimental results (reprinted with permission from King et al., 2018). All the wake structures are at t/T = 0.

Table 1
Cycle-averaged hydrodynamic performance for different stiffness cases. *Ch* = 0.089, 0.133, 0.178, 0.222, 0.267, 0.311, 0.356, 0.4, 0.445, 0.510.

Ch	0.089	0.133	0.178	0.222	0.267	0.311	0.356	0.400	0.445	0.510
$\overline{C_T}$	0.95	1.348	1.364	1.284	1.169	1.031	0.901	0.781	0.685	0.571
$\overline{C_{PW}}$	8.76	8.71	7.57	6.37	5.39	4.59	3.9	3.36	2.95	2.495
η	0.108	0.155	0.180	0.202	0.217	0.225	0.231	0.232	0.232	0.229

thrust case and the most efficient case). It can be seen that the panel generates sinusoidal-form-like pitch motions except that the pitch motions have magnitude and phase differences with the variation of the *Ch* numbers. It is also seen that the flexibility could help the panel to generate a larger pitch angle magnitude while at the same time it will produce a larger delay between the pitch motion and the actuating motion (see Eq. (1)). Comparing Fig. 5(a), (c), (d) and (e) it can be seen that the thrust and lateral force both reaches their value peak when the pitch angle is close to its peak value while the crest of hydrodynamic power arrives a little bit later than the pitch angle does. This may because of the consumption of hydrodynamic power due to the speed-up of the pitch motion, which is also the process of releasing elastic potential energy of the torsional spring.

3.1.2. Wake features

Vortex structures, pressure distribution as well as circulations at the mid-span are plotted and compared in this section in order to build a better understanding of the propulsion performance difference.

The formation and evolution of the vortices of a baseline case (Ch = 0.178) are illustrated by the instantaneous three-dimensional vortex structures in Fig. 6. It can be seen that the panel generates a series of vortex tubes and each of them contains one trailing edge vortex (TEV) and one pair of tip vortexes (TVs). The trailing edge vortex undergoes a quick spanwise compression and deforming which may due to the induce of the rotational flow from the stream-wise tip vortexes as well as the stretching of the tip vortexes. The TEV and TVs quickly merged together and then forms the long and very much twisted vortex tubes. Fig. 7 gives the comparison of the three-dimensional vortex structures for the three cases at t/T = 0. The red arrows label the vortex directions. The twisting of the vortex tubes can be seen clearly from the top views. In some particular cases, the vortex tubes may finally form a vortex loop as is seen in Fig. 7 (b1), but also with significant twists. The black arrows in the top views indicate the induced flows inside the vortex tubes of each pair. These induced concentrate flows or jets are thought to be the reason why the panel can generate thrust (Dong et al., 2006; Linden and Turner, 2004). By comparing the three cases we can see the vortex pattern in the stiffest case (Ch = 0.089) appeared to be more complex and loses coherence more quickly than the other two cases. Only one pair of vortex tubes can be seen in this case while two pairs of vortex tubes kept coherence in the other two cases.

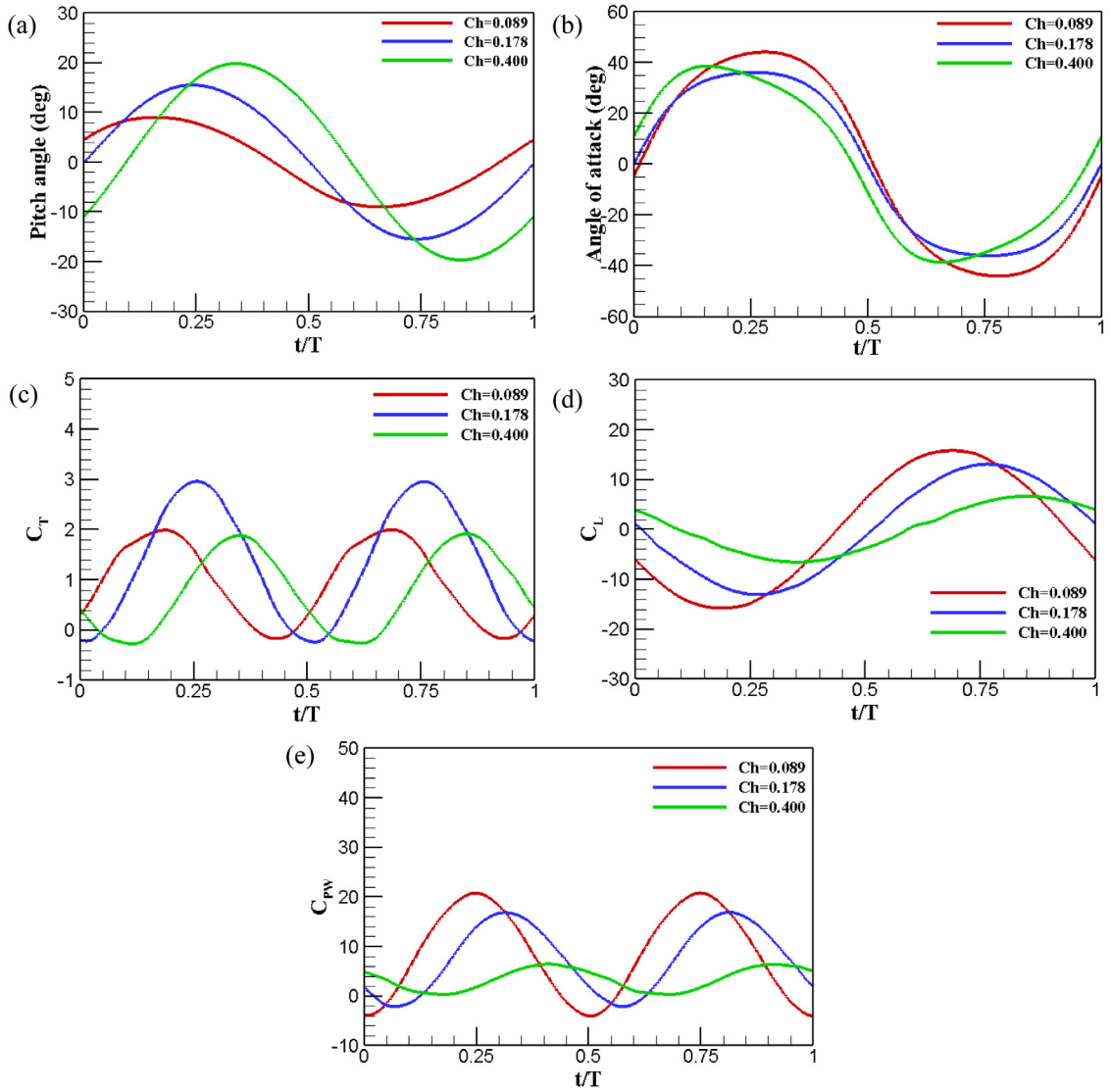

Fig. 5. Passive pitch kinematics and hydrodynamic performance in one full cycle for the Ch = 0.089, 0.178, 0.400 cases (the stiffest one, maximum thrust one and most efficient one). (a) Pitch angle (deg); (b) thrust coefficient; (c) lateral force coefficient; (d) hydrodynamic power coefficient; (e) angle of attack.

In addition, the differences in the delay of the pitch motion are also represented by the generation of each trailing edge vortex. In the most hydrodynamic efficient case (also the most flexible one in the three cases, Ch = 0.4), the newly generated TEV is just about to be detached from the trailing edge while in the other two cases the TEV has already been detached from the trailing edge.

Fig. 8 gives the flow vectors and the span-wise vorticity plot on the mid-span section at the timing of each cases' thrust peak. The free-stream velocity has been subtracted for the flow vectors. A couple of reversed vortexes can be seen downstream of the panel. Due to the compression of the TEV, the tip vortex (TV) has become dominant in the vortex tubes and only 2 or 4 TEVs can be identified clearly in the section. The vorticities coming from the tip vortexes make the pattern more complex.

The thrust generation of the flapping panels are subject to many aspects, e.g. lift-based mechanisms, added mass effects, viscous drag, and body–wake interaction, etc. (Chin and Lentink, 2016). In the current study, we mainly focus on the first two aspects. During the translation and pitching motion, the panel holds a large angle of attack most of the time. The large angle of attack lets the panel generate a lift force which is normal to the local incoming flow. The projection of the lift force in the upstream direction contributes to the thrust production of the panel. Because of the dynamic process of the pitch motion, the stall is absent. In the meanwhile, the acceleration of the panel will accelerate the water around the panel, which also contributes to the generation of thrust and is called the "added mass" effects. In consideration of the

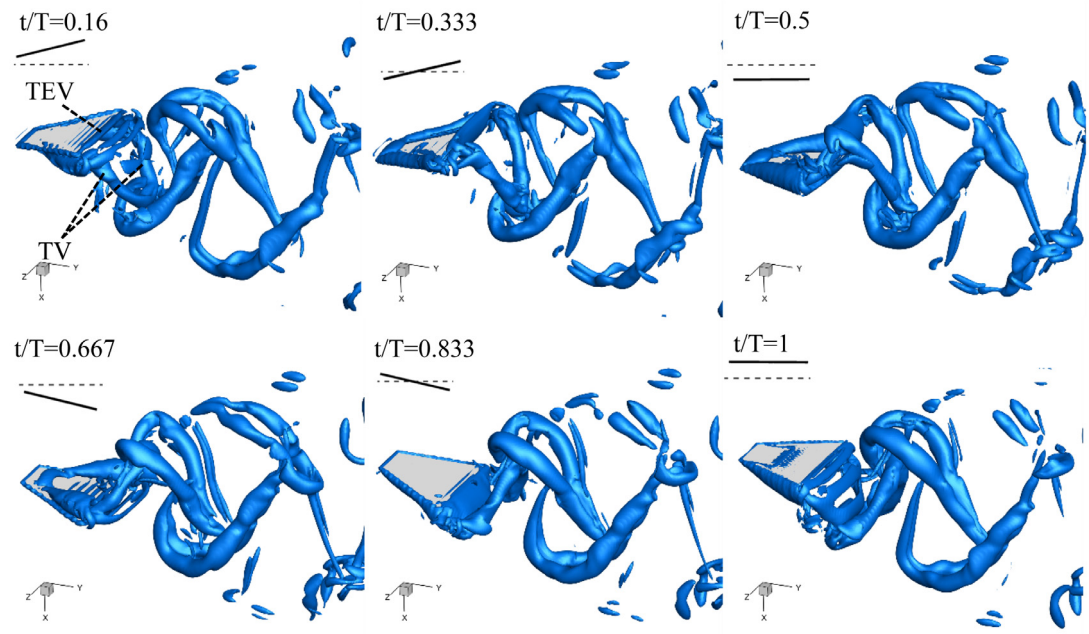

Fig. 6. Instantaneous three-dimensional vortex structures in one cycle for the case of Ch = 0.178. The vortex structure is visualized by isosurface of Q = 30.

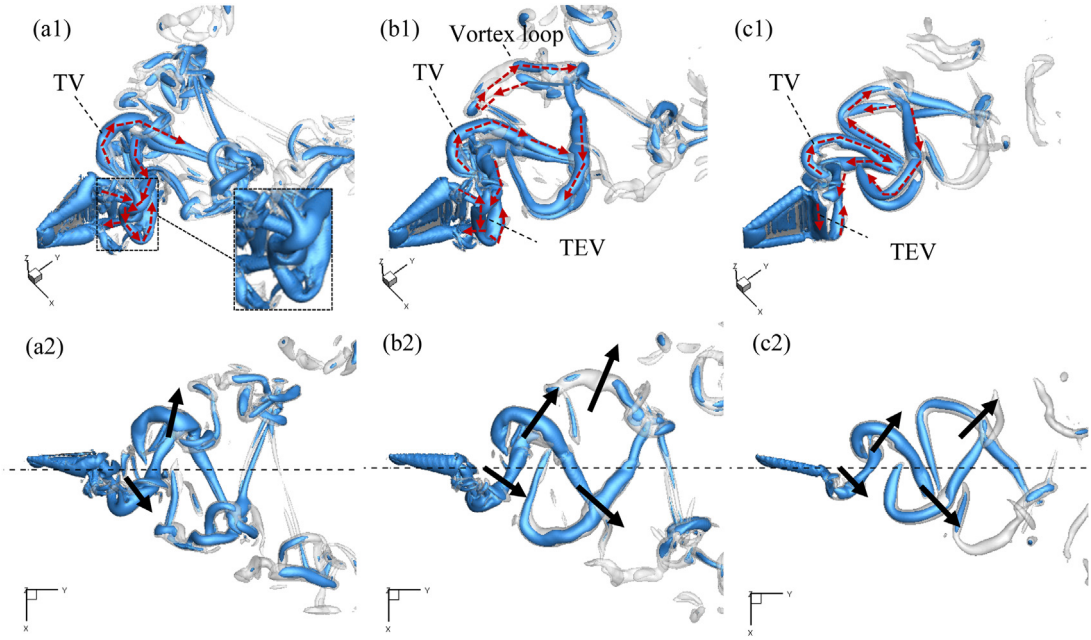

Fig. 7. Three-dimensional wake structures for Ch = 0.089, 0.178, 0.4 cases (Ch = 0.089 (a1, a2), Ch = 0.178 (b1, b2) and Ch = 0.4 (c1, c2), in which a1, b1, c1 are perspective views and a2, b2, c2 are top views) at $t/T = 0$ (start of the stroke). Wake structure is visualized by isosurface of Q criterion. Blue is for Q = 30 and gray is for Q = 10. (For interpretation of the references to color in this figure legend, the reader is referred to the web version of this article.)

translational and rotational motion in the current scenario, the added mass effects are composed of the translational part and rotational part.

Due to the different delay of the pitching motion, the panels of the three cases experience different dynamic processes. At the timing of thrust peak, the panel in the Ch = 0.089 case is in the process of accelerating to the mid-stroke, so

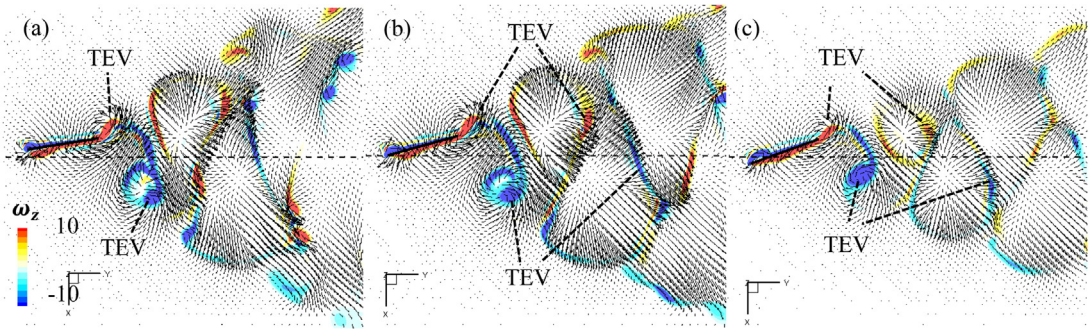

Fig. 8. Spanwise vorticity distribution and vector on the mid-span section. Each at the timing of peak thrust point. (a) Ch = 0.089, pitch angle θ = 8.9°. (b) Ch = 0.178, pitch angle θ = 15.5°. (c) Ch = 0.400, pitch angle θ = 19.8°. The free-stream velocity has been subtracted.

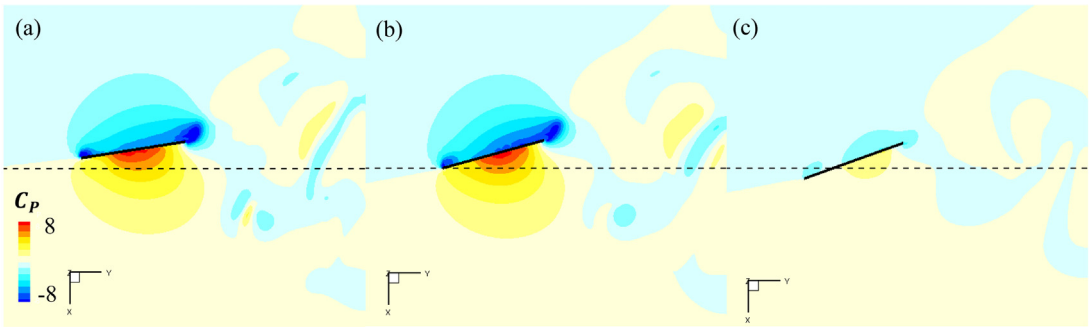

Fig. 9. Flow field pressure distribution at the thrust peak point on the mid-span section. (a) Ch = 0.089. (b) Ch = 0.178. (c) Ch = 0.4. The pressure is normalized by $0.5\rho U_\infty^2$.

the panel may under a stronger added mass effect of the translational part. Whereas in the Ch = 0.178 case, the panel is happened to be at the mid-stroke at that time, so the panel may under zero translational added mass effect at the moment, while in the Ch = 0.4 case, the panel has already passed the mid-stroke thus the panel may under a negative translational added mass effect. On the other hand, as mentioned above, all the three cases are at the timing of their pitch angle peak, so all of the panels are just about to rotate back to their equilibrium position ($\theta = 0°$), thus they are all under the added mass effect of the rotational part. Quantitatively get the volumes of these effects are difficult. Nevertheless, we give the pressure distribution around the panel and the circulation of the new shed trailing edge vortex in the mid-span section in Fig. 9 and Fig. 10 respectively. Note the circulation is calculated by integration along a closed iso-line of a certain vorticity value. It can be seen that in the first two cases, the circulations of the nearest TEV at their thrust peak point are both obviously larger than that of the third case. This explains why the pressure differences between the pressure side and the suction side of the first two cases are both larger than that of the last case as is seen in Fig. 9. In addition, the pitch angle of the second case is in between those of the other two cases, thus the forward component of the pressure difference or in other words the thrust of the second case is, therefore, the largest.

3.2. Tunable stiffness effects

From the constant stiffness results in Table 1 and Fig. 5, we can see that flexibility (large pitch angle) can benefit efficiency while possessing some extent of stiffness can help to generate more thrust. Therefore, in the tunable stiffness study, we want to prolong the period that the panel has large pitch angles, and also decrease the lateral force in the mid-stroke, thus the efficiency may be improved. So the spring stiffness is expected to be tuned to a lower value in the mid-strokes. On the other hand, we want to maintain the cycle-averaged stiffness since if we decrease the stiffness in the full cycle, the panel may not have enough elastic energy to push the water in the pitching motion just like the low constant stiffness cases in the above section, so we employ a cosinusoidal form stiffness profile that has the trough in mid-stroke and the crest at maximum-stroke. Thus the period is set to be the same with that of each stroke (half that of the oscillation cycle). The tunable stiffness is also expressed by the non-dimensional Cauchy number and is described as,

$$Ch = \frac{\rho(U^2 + V^2)c^3}{G_0 + G_k \cos(4\pi f t + \varphi)} \tag{6}$$

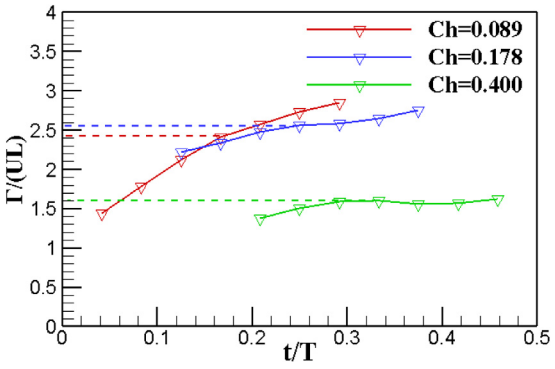

Fig. 10. Comparison of the circulation of the nearest TEV to the trailing edge.

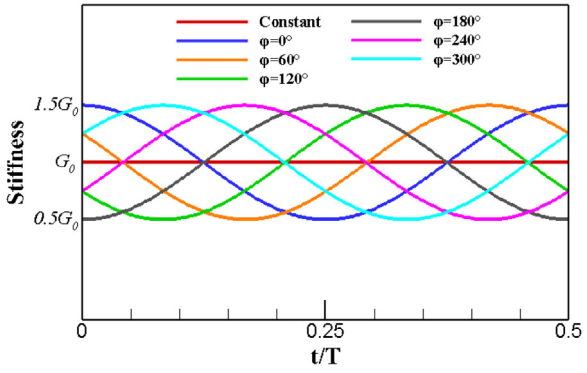

Fig. 11. Variations of stiffness over time. $G_k = 0.5G_0$.

where G_0 is the time-averaged stiffness in one full cycle. G_k is the stiffness fluctuation amplitude. In the present work, G_0 is set to be the stiffness of the Ch = 0.178 case in which the panel generates the maximum cycle averaged thrust in the constant stiffness cases. As part of the parametric study and also in search of the possible better performance, six stiffness profiles are carried out which individually has a different phase difference (φ) between the employed stiffness profile and the oscillating motion. The six profiles or cases are expressed as$\varphi = 0°, 60°, 120°, 180°, 240°, 300°$. Specifically, the $\varphi = 0°$ profile represents the profile which is mentioned above, in which the stiffness is enlarged in maximum stroke and weakened in mid-stroke. The G_k in this section is set to be half of G_0. The six stiffness profiles are shown in Fig. 11. As a comparison, the constant stiffness case Ch = 0.178 is also shown in the figure. Other parameters in the simulation are kept the same with the constant stiffness cases in the above section.

3.2.1. Kinematics and hydrodynamics

Firstly, to generally evaluate the hydrodynamic performance differences, we give the time-averaged results in one full cycle in Table 2. Obvious differences can be seen in each of these non-constant stiffness cases. Among them, the $\varphi = 0°$ case got the largest hydrodynamic efficiency (increased about 11% compared with that of the constant stiffness case) and the thrust increased about 8% compared with that of the constant one. While the $\varphi = 120°$ case had the maximum thrust (increased about 41%), but the efficiency had about a 6% decrease. We will particularly focus on these two cases and their comparison with the constant stiffness case in the left of this section.

Fig. 12 shows the pitching kinematics and instantaneous hydrodynamics results. The stiffness profiles of the $\varphi = 0°$ case and $\varphi = 120°$ case are also plotted in the figure. From the pitch angle results, it can be seen that for the $\varphi = 0°$ case, the timing of the pitch angle peak has a little bit backward shift compared with the constant stiffness case while for the $\varphi = 120°$ case, it almost stayed the same with that of the constant one. At the same time, the pitch angle amplitude both have certain augment but for the $\varphi = 0°$ case, the waveform has become not very symmetric about its wave crest point. This phenomenon can also be represented in the angular acceleration profiles of the pitch angle in Fig. 12(f), in which the two angular acceleration peaks in each stroke in the $\varphi = 0°$ case have an evident difference. As for the $\varphi = 120°$ case, the pitch angle waveform has kept almost symmetric about its peak point but the wave turn has become sharper at the crests.

Fig. 12(d) shows the thrust variation over time. In the $\varphi = 120°$ case, due to the fast increase of the stiffness at mid-stroke which induces the panel to pitch back quickly to the equilibrium position, the pitch angle angular acceleration

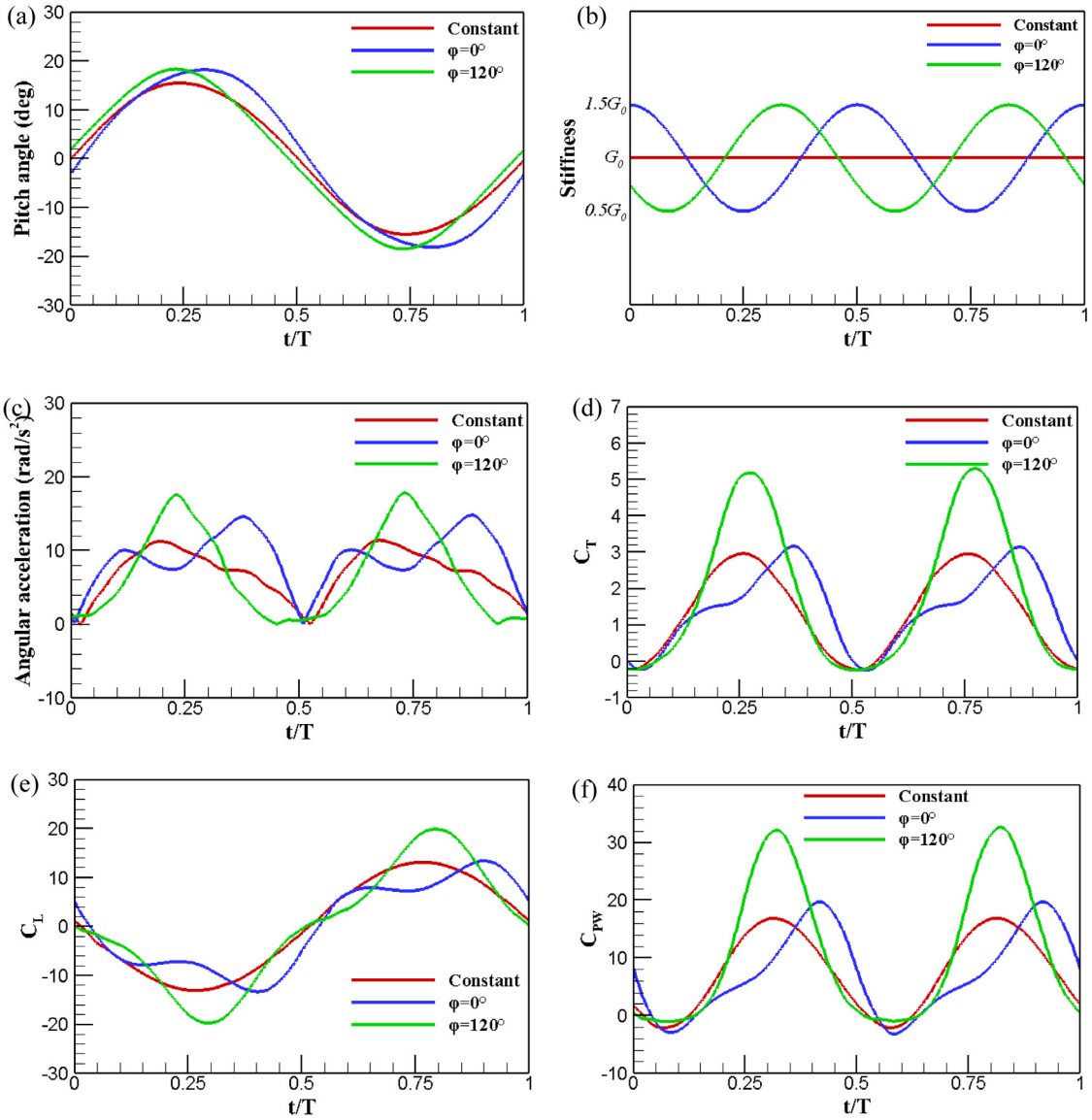

Fig. 12. Passive pitching kinematics and hydrodynamic performance in one full cycle for the $\varphi = 0°$, $\varphi = 0°$ and constant stiffness cases. (a) Pitch angle (deg). (b)Stiffness profiles. (c) Pitch angle angular acceleration (rad/s^2). (d) Thrust coefficient. (e) Lateral force coefficient. (f) Hydrodynamic power coefficient.

reaches high at mid-stroke and then lead to the thrust peak at the mid-stroke. Whereas in the $\varphi = 0°$ case, the decrease of the stiffness before mid-stroke suspended the increasing trending of the pitch angle angular acceleration and the instantaneous thrust, therefore, decelerate the growth trend while after the mid-stroke, the recovery of the stiffness accelerates the pitching progress and the thrust reaches the local crest. On the other aspect, even though the absolute pitch angle angular acceleration peak of the $\varphi = 0°$ case has an obvious argument compared with that of the constant stiffness case, the translational speed of the panel at the timing of the thrust peak is lower than that of the constant stiffness one, so the thrust peak value of the $\varphi = 0°$ case do not have evident augment compared with that of the constant stiffness case.

3.2.2. Wake features

Three-dimensional vortex structures as well as vorticity patterns and mean flows are plotted in this section aims to further the understanding of the hydrodynamic performance differences.

Fig. 13 gives the three-dimensional vortex structures for the $\varphi = 0°$, $\varphi = 120°$ and constant stiffness (Ch = 0.178) cases. It can be seen that compared with the constant stiffness case, the vortex structures of the $\varphi = 120°$ case has similar

Table 2
Cycle-averaged hydrodynamic performance for different stiffness profile cases.

Stiffness profiles	Constant	$\varphi = 0°$	$\varphi = 60°$	$\varphi = 120°$	$\varphi = 180°$	$\varphi = 240°$	$\varphi = 300°$
$\overline{C_T}$	1.364	1.475	1.819	1.921	1.497	1.092	1.035
$\overline{C_{PW}}$	7.57	7.36	10.19	11.31	9.419	6.543	5.294
η	0.180	0.200	0.178	0.17	0.159	0.167	0.196

Table 3
Cycle-averaged hydrodynamic performance for the different stiffness fluctuation amplitude cases.

Stiffness fluctuation amplitude	0	$0.25G_0$	$0.5G_0$	$0.75G_0$
$\overline{C_T}$	1.364	1.370	1.479	1.648(21% ↑)
$\overline{C_{PW}}$	7.570	7.167	7.360	8.455
η	0.180	0.191	0.200 (11% ↑)	0.195

pattern whereas big differences can be seen in that of the $\varphi = 0°$ case. In the $\varphi = 0°$ case, instead of the long and twisted vortex tubes or loops, closed round vortex loops are generated in the wake. Two major TEVs are shed in each stroke. The two major TEVs together with the tip vortexes composite the vortex loop. The vortex loops spread to opposite oscillation directions as they convect downstream.

Fig. 14 shows the spanwise vorticity and flow vectors in the mid-span section. Combining with the instantaneous vortex structures shown in Fig. 15, it can be seen that instead of two single TEVs, two pairs of counter-rotating TEVs are generated in one full cycle, which are referred to as the 2S and 2P wake configurations (Buchholz, 2006; Koochesfahani, 1989; Williamson and Roshko, 1988). From the vectors distributions on the mid-span section it is seen that in the $\varphi = 120°$ case and constant stiffness case, in addition to the induced downstream-wise flow, the vortex also induces upstream-wise flows as shown in the zoomed regions. These upstream-wise flows are thought to be inducing resistance based on Newton's third law and in the meanwhile consuming energies due to the viscous effects. However, in the $\varphi = 0°$ case, all the vortices are aligned in particular locations and avoided unprofitable vortex interactions which are appeared in the other two cases as shown in the zoomed areas. Meanwhile, all the vortices are appeared to transport the flow into the downstream which saves energies and improves efficiency.

In Fig. 16, vortex trajectories on the mid-span section are plotted using six frame spanwise vorticity plots in one full cycle and the mean flows are also plotted correspondingly. It can be seen that in the constant stiffness case and the $\varphi = 120°$ case, the main TEVs first arranged in the classic reversed Von-Karman vortex street pattern and then the TEV trajectories cross and go to the opposite directions. While in the $\varphi = 0°$ case, the TEVs generated in each stroke separate and spread to opposite directions directly after they are shed at the trailing edge and together with the other couples of TEVs in the counter strokes, they form two reversed oblique vortex streets in the separate directions. These specified vortex distributions are also represented in the mean flow pattern. In the constant stiffness case and the $\varphi = 120°$ case, a concentrated jet flow can be seen in the downstream of the panel in both of the two cases and the concentrated flow disappears downstream of the vortex trajectory cross point. While in the $\varphi = 0°$ case, a couple of separate oblique jet flows can be seen in the downstream because of the separated vortex streets. Due to the three-dimensional effects, the vortex patterns are complex and some other small features are not discussed in the paper.

3.3. Stiffness fluctuation amplitude effects

In this section, the stiffness fluctuation amplitude (G_k) effects are investigated through employing the $\varphi = 0°$ stiffness profile while G_k is set to be 0, $0.25G_0$, $0.5G_0$, $0.75G_0$ respectively. Note that $G_k = 0$ represents the constant stiffness case. The pitching kinematics, propulsion performance, surface pressure as well as wake features are given and discussed in the section.

3.3.1. Kinematics and hydrodynamics

Fig. 17 shows the pitching kinematics and hydrodynamic performance of the different G_k cases. It can be seen that the pitch angle amplitude increases as G_k improves and in the meanwhile, the timing of the pitch angle peak shifts backward. The peak thrust also increases when G_k improves except the $G_k = 0.25G_0$ case. Table 3 shows the cycle-averaged propulsion performance of the four cases. It can be seen that the mean thrust improves as G_k increases and at the same time the mean hydrodynamic power decreased in the $G_k = 0.25G_0$ and $G_k = 0.5G_0$ cases but increased in the $G_k = 0.75G_0$ case. The hydrodynamic efficiency improved in all the non-constant cases and among them the $G_k = 0.5G_0$ case stands for the most hydrodynamic efficient one. The change trending of the instantaneous hydrodynamics is consistent. The thrust and lateral force both decreased at mid-stroke whereas increased after the mid-stroke (at about 3/4 of each stroke) due to the storing and release of the stored energy respectively. Note that the decrease and increase of the stiffness are actually storing and releasing energy processes considering the elastic potential energy of the spring is $PE = \frac{1}{2}G(\Delta x)^2$, where G stands for stiffness and Δx is displacement of the torsional spring.

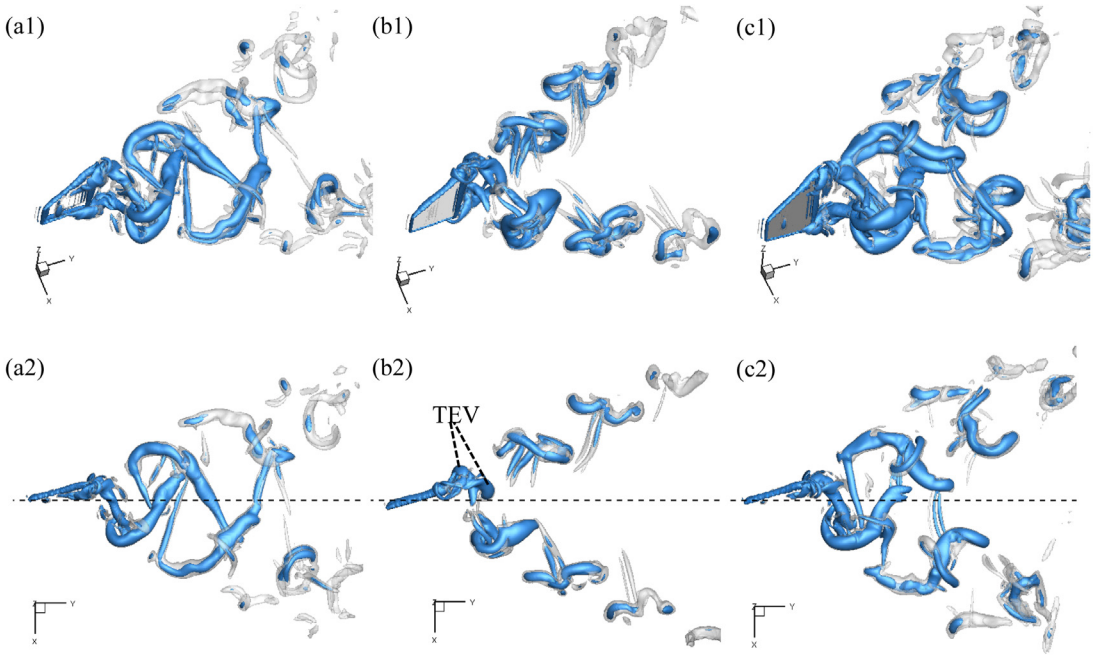

Fig. 13. Three-dimensional vortex structures at the timing of each case's instantaneous thrust peak. (a1, a2) constant stiffness. (b1, b2) $\varphi = 0°$. (c1, c2) $\varphi = 120°$. Vortex structure is visualized by isosurface of Q criterion. Blue is for Q = 30 and gray is for Q = 10. (For interpretation of the references to color in this figure legend, the reader is referred to the web version of this article.)

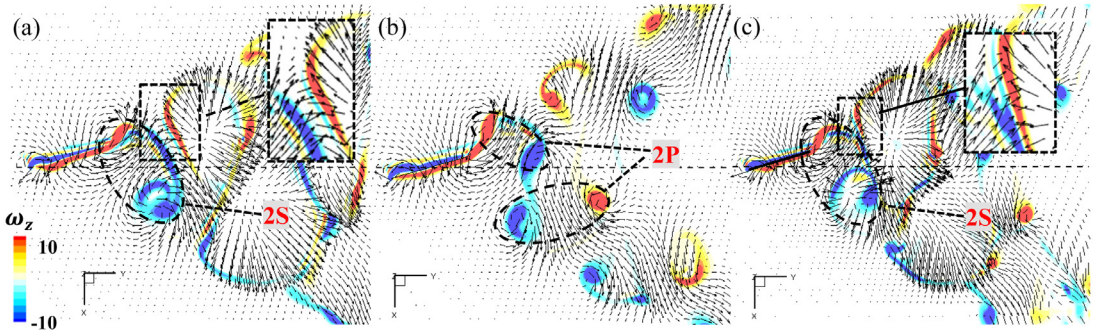

Fig. 14. Flow vectors and span-wise vorticity on the mid-span section. Each at the timing of their instantaneous thrust peak. The free-stream velocity has been subtracted. (a) constant stiffness. (b) $\varphi = 0°$. (c) $\varphi = 120°$.

3.3.2. Surface pressure and wake features

To probe the details about the performance, surface pressure and flow features are given in this section. Fig. 18 shows the surface pressure of the panel for the different stiffness fluctuation amplitude cases. Each case is at the timing of its corresponding instantaneous thrust peak. Through comparison, it is easy to distinguish that the $G_k = 0.5G_0$ and $G_k = 0.75G_0$ cases apparently have greater suction and pressure effects than the $G_k = 0.25G_0$ case. This may due to the angular accelerations of the pitch angle at the corresponding moments of these two cases are both larger than that of the $G_k = 0.25G_0$ case and thus they have greater added mass effects from the rotational part. On the other side, although the $G_k = 0.25G_0$ case has quite comparable value of pitch angle angular acceleration compared with that of the constant stiffness case at the corresponding thrust peak point, the translational speed of the $G_k = 0.25G_0$ case is less than that of the constant stiffness case at that moment since it has already passed the mid-stroke. So the suction and pressure effects of the constant stiffness case are also greater than the $G_k = 0.25G_0$ case. This is also represented in the angle of attack difference, the angle of attack of the constant stiffness case at the corresponding point is apparently greater than that of the $G_k = 0.25G_0$ case due to the larger translational speed.

Differences in the suction and pressure effects are also seen in the comparison between the $G_k = 0.5G_0$ case and the $G_k = 0.75G_0$ case. Larger suction areas can be seen in the $G_k = 0.5G_0$ case at the swept edge areas. The suction at this area is commonly induced by the streamwise swept edge vortexes which are generated by the translational flows at the

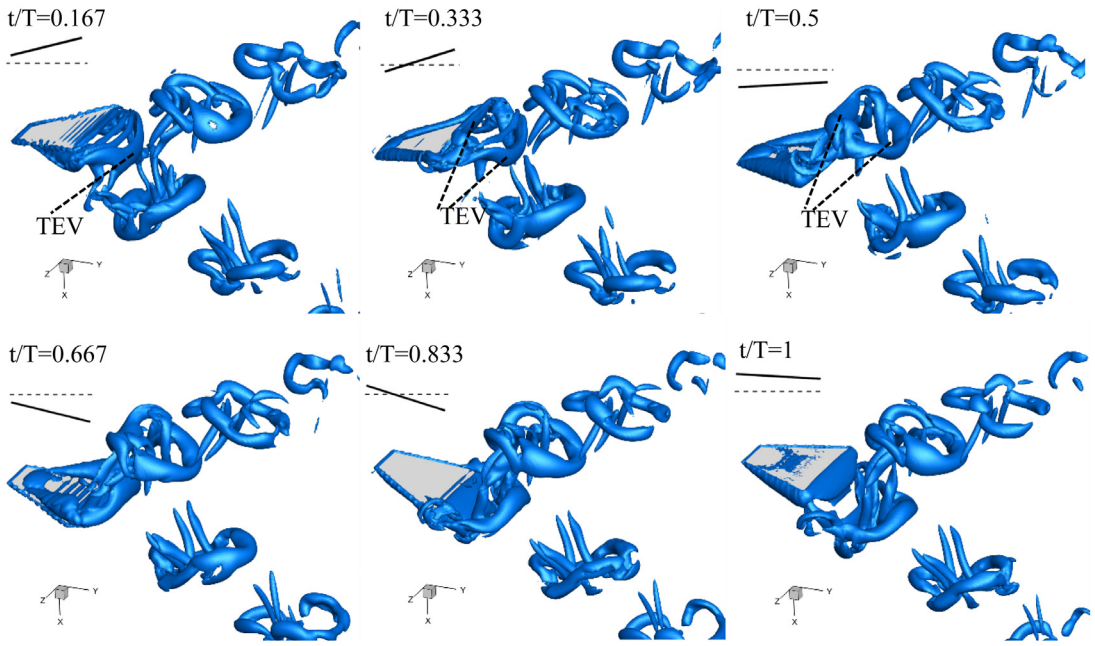

Fig. 15. Instantaneous three-dimensional vortex structures in one cycle for the $\varphi = 0°$ case. The vortex structure is visualized by isosurface of Q = 30.

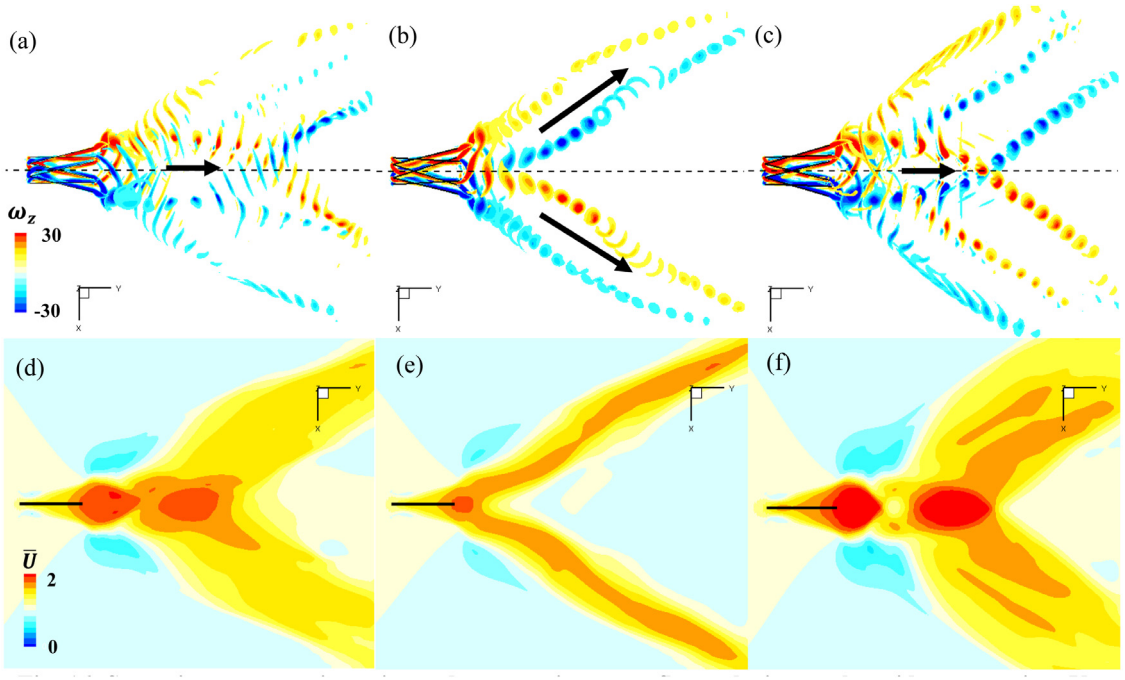

Fig. 16. Spanwise vertex trajectories and streamwise mean flow velocity on the mid-span section. Vortex trajectories: (a) constant stiffness, (b) $\varphi = 0°$, (c) $\varphi = 120°$; streamwise mean flow velocity: (d) constant stiffness, (e) $\varphi = 0°$, (f) $\varphi = 120°$ respectively. The mean flow velocity is normalized by the incoming flow velocity U_∞.

swept edges. From Fig. 17(e) we can see that at the corresponding time, the angle of attack of the $G_k = 0.5G_0$ case is larger than the $G_k = 0.75G_0$ case and the larger angle of attack induces larger pressure difference between the suction side and pressure side of the panel and thus induces stronger streamwise vortexes at the swept edge as is seen in Fig. 19.

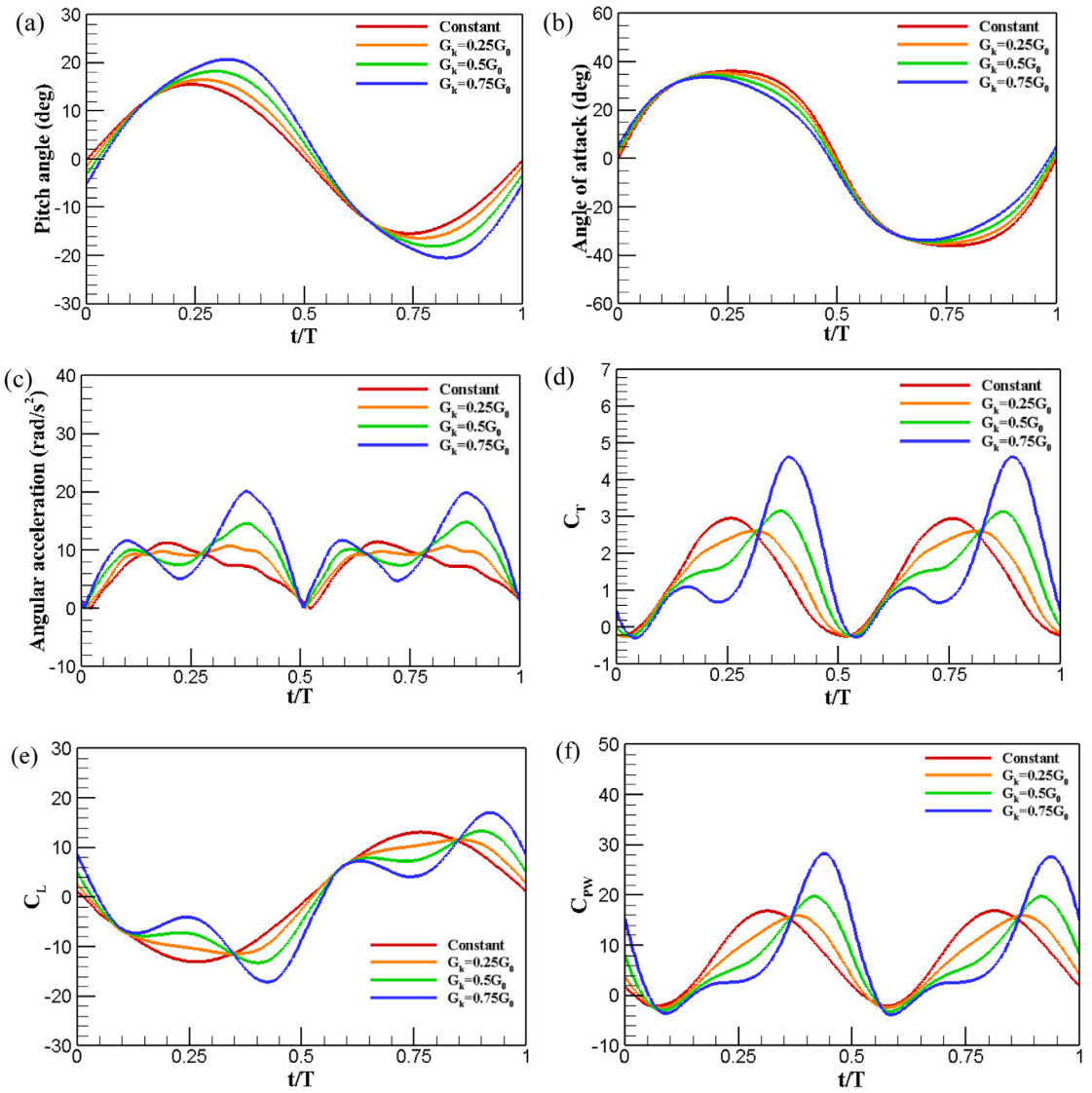

Fig. 17. Pitching kinematics and hydrodynamic performance in one full cycle for the different stiffness fluctuation amplitude cases. (a) Pitch angle (deg). (b) Angle of attack (deg). (c) Pitch angle angular acceleration (rad/s^2, absolute value). (d) Thrust coefficient. (e) Lateral force coefficient. (f) Hydrodynamic power coefficient.

On the other aspect, due to the larger pitch angle acceleration, the panel in the $G_k = 0.75G_0$ case has larger added mass effect of the rotation part and thus induces greater suction and pressure effects in the near mid-span area.

Three-dimensional vortex structures and flow vectors as well as spanwise vorticities on the mid-span section for the three non-constant stiffness cases are shown in Fig. 20. It can be seen that in the $G_k = 0.25G_0$ case, the vortexes did not form the entire vortex loops like in the $G_k = 0.5G_0$ case. Instead, it kept some features of the constant stiffness cases which are the formation of the long and twisted vortex tubes that are composed by the tip vortexes and the compressed trailing edge vortexes. Nevertheless, instead of a single vortex tube, the panel generates a pair of vortex tubes in each stroke. The vortex tubes in each pair interconnected with each other form a more complex pattern. Whereas, in the $G_k = 0.75G_0$ case, similar vortex loops can be found compared with the $G_k = 0.5G_0$ case in spite of the vortex loops have a little bit orientation difference and long legs can be seen in each vortex loops. From the flow vectors on the mid-span section, it can be seen that in the $G_k = 0.75G_0$ case, the vortices still hold a 2P pattern as in the $G_k = 0.5G_0$ case whereas the arrangement has some difference. For the vortexes that are close to the panel, the inner parts (the parts that are more close to the dashed line) of the pairs of the vortexes are too close to each other and thus induces upstream flows as shown by the arrows in Fig. 20(f). This is a phenomenon of drag production and power consumption and may explain why the hydrodynamic efficiency is decreased compared with that of the $G_k = 0.5G_0$ case.

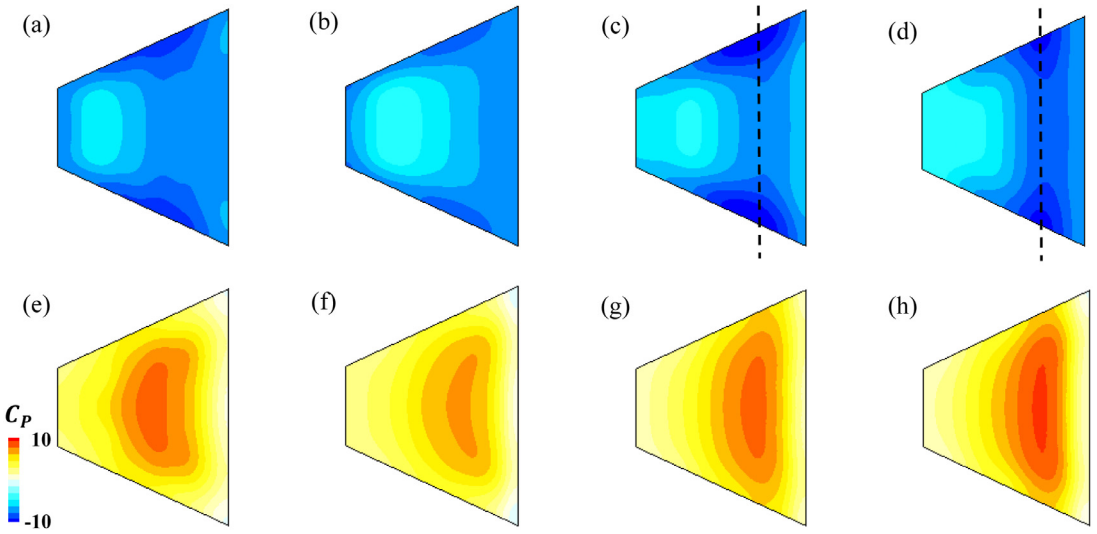

Fig. 18. Surface pressure of the panel for the different stiffness fluctuation amplitude cases at the timing of each case's thrust peak. (a, e) $G_k = 0$; (b, f)$G_k = 0.25G_0$; (c, g) $G_k = 0.5G_0$; (d, h) $G_k = 0.75G_0$. The upper and bottom are suction side and pressure side, respectively.

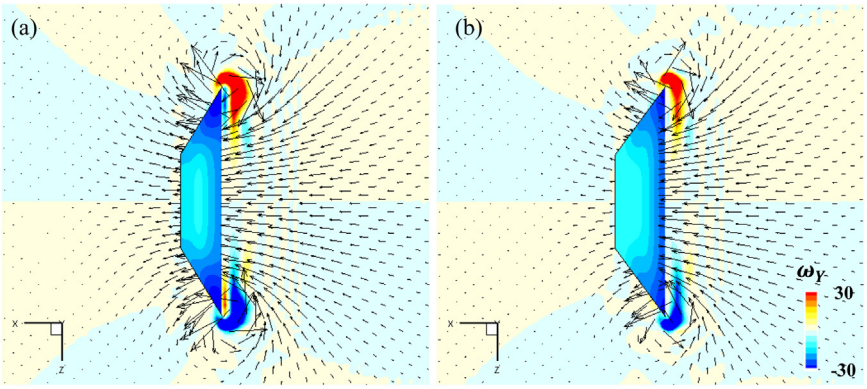

Fig. 19. Streamwise vorticity distribution and flow vectors at the streamwise section of the (a) $G_k = 0.5G_0$ and (b) $G_k = 0.75G_0$ cases. The section position is indicated by the dashed line shown in Fig. 18(c) and (d). Surface pressure is also plotted on the panel and scale is the same as Fig. 18.

3.4. Applicability for motions with different oscillating amplitudes

In the above sections, we have investigated the effects of constant and tunable stiffness with phase shift and amplitude difference on the performance of the propulsor. But they are all under the same oscillating amplitude motion. In this section, we study the tunable stiffness beneficial applicability for different oscillating amplitude motions. The ratio of oscillating motion amplitude to chord A^* has been changed to 0.6 and 0.8, respectively. The Reynolds number, reduced frequency, and Mass number are kept the same with that in the above sections and the stiffness fluctuation amplitudes G_k are set to be half of the cycle averaged stiffness G_0 and each G_0 is set to be the value with which if the stiffness is constant, the Cauchy number will be 0.178, in which case the panel acquires the largest thrust in the constant stiffness cases. The phase difference between the stiffness profiles and oscillating motion φ is set to be 0 since under this scenario the propulsion performance has benefits in both mean thrust and efficiency in the above cases.

Table 4 shows the propulsion performance under motions with different A^*. It can be seen that in all these three scenarios the mean thrust and hydrodynamic efficiency have been enhanced. Among them, in the $A^* = 0.8$ scenario, the efficiency has the largest augment, approximately 16% improvement compared with the constant stiffness case. In the $A^* = 0.4$ scenario, the panel has the largest improvement in mean thrust (8%). These data indicate that employing this kind of tunable stiffness can benefit the propulsion performance in a certain range of oscillating amplitudes.

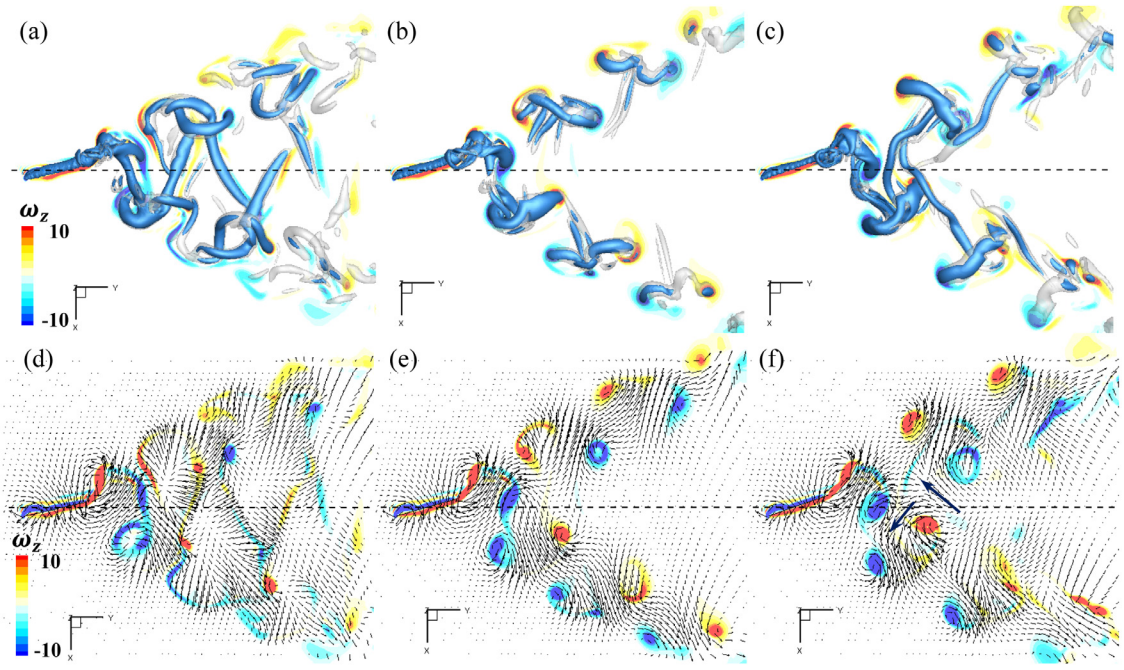

Fig. 20. Three-dimensional vortex structures, flow vectors and spanwise vorticities on the mid-span section for the three different stiffness fluctuation amplitude cases. (a, d) $G_k = 0.25G_0$; (b, e)$G_k = 0.5G_0$; (c, f)$G_k = 0.75G_0$. The vortex structures are visualized by isosurface of Q criterion. The blue layer stands for Q = 30 and the gray layer stands for Q = 10. (For interpretation of the references to color in this figure legend, the reader is referred to the web version of this article.)

Table 4
Performance under motions with different oscillating amplitudes.

A^*	0.4		0.6		0.8	
Stiffness profiles	Constant	Tunable	Constant	Tunable	Constant	Tunable
$\overline{C_T}$	1.364	1.475 (8% ↑)	2.874	2.907 (1% ↑)	4.273	4.427 (4% ↑)
$\overline{C_{PW}}$	7.570	7.360	21.87	19.39	43.17	38.45
η	0.180	0.200 (11% ↑)	0.131	0.150 (15% ↑)	0.099	0.115 (16% ↑)

4. Conclusion

In the present study, three-dimensional numerical simulations are carried out to study the propulsion performance and flow features of a torsional-spring-derived passive pitching panel. The torsional spring stiffness effects have been put emphases on and a real-time altering stiffness idea is pointed out and employed in the study.

The research found that employing constant stiffness may let the panel generate sinusoidal-form-like pitch motions in spite of that the pitching amplitudes and phase lags with the driving motion may be different with the variation of the stiffness. Flexibility may help the panel obtain high efficiency while holding some extent of stiffness help the panel generate more thrust. Under the current set up (panel shape, reduced frequency, etc.) the panel generates the maximum cycle-averaged thrust when Ch number is close to 0.178 and has the maximum hydrodynamic efficiency when Ch number is near 0.4. When Ch = 0.178, the panel possesses a large angle of attack at mid-stroke which helps the circulation of the panel maintain large while at the same time the pitch angle is enough high among the tested cases, and thus this case got the highest thrust.

A real-time tunable stiffness strategy is pointed out in the paper. The stiffness of the torsional spring changes as a function of the driving motion. A cosinusoidal waveform is employed in the stiffness profiles. The waveform period is set to be half of that of the oscillation motion since each oscillation contains two strokes. First, six phase different stiffness profile cases are tested. Results show that in the tested six cases, the $\varphi = 0^\circ$ case (in-phase with the oscillation) shows the best efficiency enhancement and at the same time it also acquires augment in cycle averaged thrust. On the other side, the $\varphi = 120^\circ$ case (out-of-phase) has the maximum thrust improvement but has a certain loss in efficiency. The flow pattern shows that instead of the long and twisted vortex tubes that are seen in the constant stiffness cases, the panel generates couples of round and closed vortex loops in the $\varphi = 0^\circ$ case. The vortex loops separate and spread in the opposite oscillation directions directly after they have been detached from the panel. The vortexes have fewer interactions

compared with the vortex tubes in the constant stiffness cases and all the vortices are appeared to induce the flows into downstream which helps generate thrust. While on the other side, in the $\varphi = 120^\circ$ and the constant stiffness cases, the vortices show quite a few unprofitable interactions and also induce upstream flows that produce resistance and consume energy.

The effects of the stiffness fluctuation amplitude (G_k) are also studied. Three levels of G_k cases ($G_k = 0.25G_0$, $G_k = 0.5G_0$, $G_k = 0.75G_0$, where G_0 stands for the time-averaged stiffness and equals to the stiffness of the Ch = 0.178 case) are investigated in the study. Mean thrust and hydrodynamic efficiency of the three cases are all increased and among them the $G_k = 0.75G_0$ case acquired the maximum augment in generating thrust while the $G_k = 0.5G_0$ case possesses the largest hydrodynamic efficiency. The flow patterns show that in the $G_k = 0.25G_0$ case the panel generates two trailing edge vortexes in each stroke just like in the $G_k = 0.5G_0$ case but the corresponding vortex tubes did not form a similar vortex loop and instead, the vortex tubes interconnected with each other showing a complex configuration as they convect downstream. Whereas in the $G_k = 0.75G_0$ case, similar vortex loops are seen as in the $G_k = 0.25G_0$ case nevertheless the vortex loops have orientation differences. The vorticity distribution on the mid-span section shows that the inner parts of the pairs of the vortices are closer to each other compared with that in the $G_k = 0.5G_0$ case and thus induces upstream flows which lead to drag production and power consumption. This is also thought to be the reason why the hydrodynamic efficiency of the $G_k = 0.75G_0$ case is lower than that of the $G_k = 0.5G_0$ case. Cases with motions with different oscillating amplitudes are also carried out. The results show that employing this kind of real-time altering stiffness ($\varphi = 0^\circ, G_k = 0.5G_0$) can benefit the propulsion performance in motions with a certain range of oscillating amplitudes ($0.4 \leq A^* \leq 0.8$).

On the other hand, based on the findings in the study, the mechanism of the improvement of hydrodynamic efficiency when employing the tunable stiffness is that the vortices generated in each cycle are in a particular sequence which forms a pattern that avoided unprofitable interactions. From this point of view, when employing a fully flexible panel propulsor, using this kind of tunable stiffness may also help, but it depends on the wake profiles that the panel has formed.

Declaration of competing interest

The authors declare that they have no known competing financial interests or personal relationships that could have appeared to influence the work reported in this paper.

Acknowledgments

This work was supported in part by the Office of Naval Research MURI Grant N000141410533 and NSF CNS-1931929 to HD, and China scholarship council and National Natural Science Foundation of China (11972060 & 1721202) to HH and YW.

References

Adams, D.S., Fish, F.E., 2019. Odontocete peduncle tendons for possible control of fluke orientation and flexibility. J. Morphol. 280, 1323–1331.
Bergou, A.J., Xu, S., Wang, Z.J., 2007. Passive wing pitch reversal in insect flight. J. Fluid Mech. 591, 321–337.
Buchholz, J.H., 2006. The Flowfield and Performance of a Low Aspect Ratio Unsteady Propulsor. Princeton University, New Jersey.
Chin, D.D., Lentink, D., 2016. Flapping wing aerodynamics: from insects to vertebrates. J. Exp. Biol. 219, 920–932.
Daniel, T.L., Combes, S.A., 2002. Flexible wings and fins: bending by inertial or fluid-dynamic forces? Integr. Comp. Biol. 42, 1044–1049.
Dong, H., Liang, Z., Harff, M., 2009. Optimal settings of aerodynamic performance parameters in hovering flight. Int. J. Micro Air Veh. 1, 173–181.
Dong, H., Mittal, R., Najjar, F., 2006. Wake topology and hydrodynamic performance of low-aspect-ratio flapping foils. J. Fluid Mech. 566, 309–343.
Fish, F.E., Nusbaum, M.K., Beneski, J.T., Ketten, D.R., 2006. Passive cambering and flexible propulsors: cetacean flukes. Bioinspir. Biomimetics 1 (S42).
Floryan, D., Van Buren, T., Rowley, C.W., Smits, A.J., 2017. Scaling the propulsive performance of heaving and pitching foils. J. Fluid Mech. 822, 386–397.
Ishihara, D., Yamashita, Y., Horie, T., Yoshida, S., Niho, T., 2009. Passive maintenance of high angle of attack and its lift generation during flapping translation in crane fly wing. J. Exp. Biol. 212, 3882–3891.
Khalid, Muhammad Saif Ullah, Wang, Junshi, Dong, Haibo, Liu, Moubin, 2020. Flow transitions and mapping for undulating swimmers. Phys. Rev. Fluids 5 (6), 063104.
King, J.T., Kumar, R., Green, M.A., 2018. Experimental observations of the three-dimensional wake structures and dynamics generated by a rigid, bioinspired pitching panel. Phys. Rev. Fluids 3, 034701.
Koochesfahani, M.M., 1989. Vortical patterns in the wake of an oscillating airfoil. AIAA J. 27, 1200–1205.
Li, C., Dong, H., 2016. Three-dimensional wake topology and propulsive performance of low-aspect-ratio pitching-rolling plates. Phys. Fluids 28, 071901.
Li, C., Dong, H., 2017. Wing kinematics measurement and aerodynamics of a dragonfly in turning flight. Bioinspir. Biomimetics 12, 026001.
Li, C., Dong, H., Liu, G., 2015. Effects of a dynamic trailing-edge flap on the aerodynamic performance and flow structures in hovering flight. J. Fluids Struct. 58, 49–65.
Linden, P., Turner, J., 2004. 'Optimal' vortex rings and aquatic propulsion mechanisms. Proc. R. Soc. B 271, 647–653.
Liu, G., Ren, Y., Dong, H., Akanyeti, O., Liao, J.C., Lauder, G.V., 2017. Computational analysis of vortex dynamics and performance enhancement due to body–fin and fin–fin interactions in fish-like locomotion. J. Fluid Mech. 829, 65–88.
Mittal, R., Dong, H., Bozkurttas, M., Najjar, F., Vargas, A., Von Loebbecke, A., 2008. A versatile sharp interface immersed boundary method for incompressible flows with complex boundaries. J. Comput. Phys. 227, 4825–4852.
Moore, M.N.J., 2014. Analytical results on the role of flexibility in flapping propulsion. J. Fluid Mech. 757, 599–612.
Sum Wu, K., Nowak, J., Breuer, K.S., 2019. Scaling of the performance of insect-inspired passive-pitching flapping wings. J. R. Soc. Interface 16, 201906.
Wan, H., Dong, H., Gai, K., 2015. Computational investigation of cicada aerodynamics in forward flight. J. R. Soc. Interface 12, 20141116.

Wang, J., Han, P., Zhu, R., Liu, G., Deng, X., Dong, H., 2018. Wake capture and aerodynamics of passively pitching tandem flapping plates. In: 2018 Fluid Dynamics Conference, p. 3236.
Wang, J., Ren, Y., Li, C., Dong, H., 2019. Computational investigation of wing-body interaction and its lift enhancement effect in hummingbird forward flight. Bioinspir. Biomimetics 14, 046010.
Wang, Junshi, Wainwright, Dylan, Lindengren, Royce, Lauder, George, Dong, Haibo, 2020. Tuna locomotion: a computational hydrodynamic analysis of finlet function. J. Royal Soc. Interface 17 (165), 20190590.
Whitney, J.P., Wood, R.J., 2010. Aeromechanics of passive rotation in flapping flight. J. Fluid Mech. 660, 197–220.
Williamson, C.H., Roshko, A., 1988. Vortex formation in the wake of an oscillating cylinder. J. Fluids Struct. 2, 355–381.
Wood, R.J., 2008. The first takeoff of a biologically inspired at-scale robotic insect. IEEE Trans. Robot. 24, 341–347.
Zeyghami, S., Zhong, Q., Liu, G., Dong, H., 2018. Passive pitching of a flapping wing in turning flight. AIAA J. 1–9.
Zhong, Q., Dong, H., Quinn, D.B., 2019. How dorsal fin sharpness affects swimming speed and economy. J. Fluid Mech. 878, 370–385.
Zhong, Q., Liu, G., Ren, Y., Dong, H., 2017. On the passive pitching mechanism in turning flapping flights using a torsional spring model. In: 47th AIAA Fluid Dynamics Conference, p. 3817.
Zhu, J., White, C., Wainwright, D., Di Santo, V., Lauder, G., Bart-Smith, H., 2019. Tuna robotics: A high-frequency experimental platform exploring the performance space of swimming fishes. Sci. Robot. 4, eaax4615.